JOURNAL OF SOLID STATE CHEMISTRY 139, 362–372 (1998)
ARTICLE NO. SC987858

Characterization of New Lead-Based Monophosphate Tungsten Bronzes, $Pb_x(PO_2)_4(WO_3)_{2m}$ ($6 \leq m \leq 10$)

P. Roussel,[1] A. C. Masset, B. Domengès, A. Maignan, D. Groult, and Ph. Labbé

Laboratoire CRISMAT-ISMRA, Université de Caen, CNRS UMR 6508, 6 Boulevard du Maréchal Juin, 14050 Caen, France

Received February 4, 1998; accepted April 14, 1998

A new series of lead-based monophosphate tungsten bronzes ($MPTB_h$), $Pb_x(PO_2)_4(WO_3)_{2m}$, was isolated for $6 \leq m \leq 10$ and characterized by X-ray diffraction, electron microscopy, and resistivity and magnetic susceptibility measurements. The crystal structure was solved for $m = 7$ from three-dimensional single-crystal X-ray data [$Pb_{0.66}P_4W_{14}O_{50}$: triclinic, $A\bar{1}$, $a = 6.6015(3)$ Å, $b = 5.3156(4)$ Å, $c = 27.039(2)$ Å, $\alpha = 90.208(6)^\circ$, $\beta = 96.757(5)^\circ$, $\gamma = 89.867(5)^\circ$, $Z = 1$, final $R = 2.16\%$ for 4462 independent reflections with $I > 3.0\sigma(I)$]. Lead atoms are distributed in cages bounded by 18 oxygen atoms, in a part that favors a PO_4 tetrahedron neighbor rather than a WO_6 octahedron neighbor. Consequently, Pb atoms exhibit an (3+5) eightfold coordination that takes into account the $6s^2$ lone-pair stereoactivity. Resistivity measurements performed on oriented single crystals reveal quasi-two-dimensional metallic behavior for the entire temperature range investigated, 4.2 to 300 K. Magnetic susceptibility data indicate Pauli paramagnetic behavior. The results are compared with those of alkaline-based counterparts, $A_x(PO_2)_4(WO_3)_{2m}$ (A = Na, K).

INTRODUCTION

The discovery of electronic instabilities leading to a charge density wave (CDW) state in the quasi-two-dimensional (2D) monophosphate tungsten bronzes $(PO_2)_4(WO_3)_{2m}$ (1–5) has renewed the interest of these materials synthesized for the first time more than 15 years ago (6– 9).

The crystal structure has been described as built up of perovskite WO_3-type slabs joined through PO_4 tetrahedra involving pentagonal tunnels and quasi-2D electronic properties. Moreover, because they offer the possibility of changing the thickness of the WO_3-type slabs and therefore the average conduction electron density $2/m$ per W atom by playing on the m value, they have been considered as providing a model system to deepen the understanding of CDW instabilities in quasi-2D conductors.

Systematic studies of these bronzes for $4 \leq m \leq 14$ (10, 11) show that the Peierls or instability temperatures increase with m. High transition temperatures above room temperature and up to 500 K are found for $m > 8$ and explained on the basis of a strengthening of electron–electron interactions and electron–phonon coupling (12). For low m value ($m = 4$, 6) huge positive magnetoresistance effects have been observed and attributed to the coexistence of high-mobility electron and hole pockets left by the CDW gap opening at the Fermi level (2, 13).

Besides this series of $MPTB_p$ materials, there exists another series of monophosphate tungsten bronzes: the so-called $MPTB_h$, $A_x(PO_2)_4(WO_3)_{2m}$, which exhibit a closely related structure characterized by the existence of pseudo-hexagonal tunnels partly filled by the alkaline cation $A^+ = Na^+$ or K^+ (14–16). Although electronic properties of these $MPTB_h$ have not been studied as much as those of $MPTB_p$, band structure calculations carried out in a tight-binding extended Hückel approximation (17) did predict similar CDW instabilities. Resistivity measurements first reported by Wang *et al.* (18) for $Na_{1.6}P_4W_8O_{32}$ ($m = 4$) and $Na_2P_4W_{12}O_{44}$ ($m = 6$) show metallic and quasi-2D behavior with a weak, broad metal-to-metal transition at about 90 K for $m = 4$ and 140 K for $m = 6$ presumably related to Peierls transitions.

More recently the electron transport properties of large platelike crystals of $K_xP_4W_8O_{32}$ were studied for three different values of x, the potassium content (19). In contrast to the Na-based analogue, the thermal variation of the resistivity between 300 and 4.2 K reveals the existence of a single, strong anomaly whose onset temperature T_p depends on x: $T_p = 135$ K for $x = 1.00(5)$, $T_p = 150$ K for $x = 1.05(5)$, and $T_p = 170$ K for $x = 1.30(9)$. Anomalies can also be observed in the thermal dependence of the thermopower. The increase of T_p with x and therefore with the filling of the conduction band is at present not well understood. Also, it is not clear why the sodium-based compounds exhibit weaker metal-to-metal transitions compared with those of the potassium counterpart.

[1] To whom correspondence should be addressed. E-mail: p.roussel@crismat.ismra.fr. Fax: (33) 02–31–95–16–00.

0022-4596/98 $25.00

To study the effects on CDW formation of both electron band filling and possible cation ordering in hexagonal tunnels, the substitution of Pb^{2+} for Na^+ and K^+ was investigated. In this paper, we report on the structure and electrical properties of new lead-based monophosphate tungsten bronzes with hexagonal tunnels $Pb_x(PO_2)_4(WO_3)_{2m}$ with $6 \leq m \leq 10$.

EXPERIMENTAL

Sample Preparation

Mixtures of $(NH_4)_2HPO_4$, WO_3, and PbO in appropriate ratios were first heated in air at 600°C for 12 h to decompose the phosphate. Because of the mixed valency of tungsten, an adequate amount of powder metallic tungsten used as a reducing agent was added to the decomposed initial mixture before grinding intimately. Samples corresponding to the nominal compositions $Pb(PO_2)_4(WO_3)_{2m}$ ($4 \leq m \leq 13$) were then heated in evacuated silica ampoules with two steps at 800 and 900°C for 12 and 24 h, respectively.

Crystal Growth

A charge of about 2 g of well-crystallized $Pb(PO_2)_4(WO_3)_{2m}$ powder was weighed and placed in a quartz tube ~20 cm long and 1.8 cm in internal diameter that was sealed under vacuum. After the tube was placed in a horizontal furnace a temperature gradient of ~10°C/cm was applied along its length; i.e., the hot zone = 1200°C and the cold zone = 1000°C. The powder was held under these conditions for 1 week to grow single crystals by chemical transport at the cold zone.

Characterization of the Samples

X-ray powder diffraction patterns of the products were recorded with a Philips diffractometer using monochromatized Cu$K\alpha$ radiation. The quality and cell parameters of the single crystals were checked with Weissenberg photographs.

Crystal structure calculations were carried out from the data collected with a CAD4 Enraf–Nonius automated diffractometer and Mo$K\alpha$ radiation. Data collection parameters (scan width, counter slit aperture, scan type) were fixed after analysis of the shape of five reflections. The background intensity was measured on both sides of each reflection and periodic control (every 1 h) verified the crystal stability. The measured intensities were corrected for scale variations based on standard reflections and Lorentz and polarization effects. A Gaussian-type absorption correction based on the crystal morphology was then carried out and verified by applying the absorption correction on a series of psi scans taken for 25 reflections.

All refinements were performed with the JANA98 program package (20). Scattering factors for neutral atoms and the correction terms were taken from International Tables of Crystallography. Atomic parameters, scale factor, and isotropic extinction coefficient were refined in a full-matrix mode, minimizing the function Rw. A weighting scheme based on $\sigma(F_0)$ was used.

Electron diffraction investigation was performed on a JEM 200CX equipped with a tilting rotating goniometer ($\pm 60°$), and the high-resolution (HREM) study on a TOPCON2B electron microscope equipped with a $\pm 10°$ double-tilt goniometer and objective lens with spherical aberration constant of 0.4 mm. High-resolution images and convergent beam electron diffraction (CBED) patterns were calculated using the multislice and block wave methods, respectively, of the EMS package.

Conventional four-probe DC measurements were carried out on oriented crystals. Electrical contacts were made by ultrasonic soldering of indium on the surface of the crystal. Magnetic susceptibility was measured by means of a Squid magnetometer with an applied field of 0.5 T.

RESULTS

Synthesis and Electron Microscopy Studies

Several new lead-based phosphate tungsten bronzes $Pb_xP_4W_{2m}O_{8+6m}$ have been isolated as pure phases. They correspond to the terms $m = 6$, 7, 8, 9, and 10. Electron diffraction study performed on crushed single crystals corresponding to $m = 6$ and $m = 7$ samples shows in both cases a monoclinic symmetry with the following unit cell parameters: $a \approx 6.6$ Å, $b \approx 5.3$ Å, $c \approx 23.8$ Å, $\beta \approx 93°$ for $m = 6$, reflection conditions $(0k0)$, $k = 2n$; $(h0l)$, $l = 2n$, implying the space group $P2_1/c$ (Fig. 1a) and, $a \approx 6.6$ Å, $b \approx 5.3$ Å, $c \approx 27.1$ Å, $\beta \approx 96°$ for $m = 7$, reflection conditions (hkl), $k + l = 2n$, implying the possible space group $A2/m$ (Fig. 1b).

The results are in good agreement with those previously obtained for K-based and Na-based analogues, indicating that Pb-based bronzes all belong to the $MPTB_h$ series (15, 16). Unit cell parameters have been refined from powder XRD data and reported in Table 1. HREM images show contrasts similar to those observed in K-$MPTB_h$ and Na-$MPTB_h$: depending on focus value (Fig. 2) either perovskite-type and pseudo-hexagonal tunnels of the structure are imaged (−30 nm focus, low-electron-density zones highlighted) or tungsten atoms and PO_4 tetrahedra appear as bright dots (35 nm focus, high-electron-density zones highlighted).

The building principle of the $MPTB_h$ framework allows original defects to be stabilized. One example is shown in Figs. 3 and 4; it was observed in an $m = 6$ fragment. The corresponding ED pattern (Fig. 3a) can be interpreted as the superimposition of two patterns due to the existence of two distinct domains (Figs. 3b and 3c). This interpretation takes

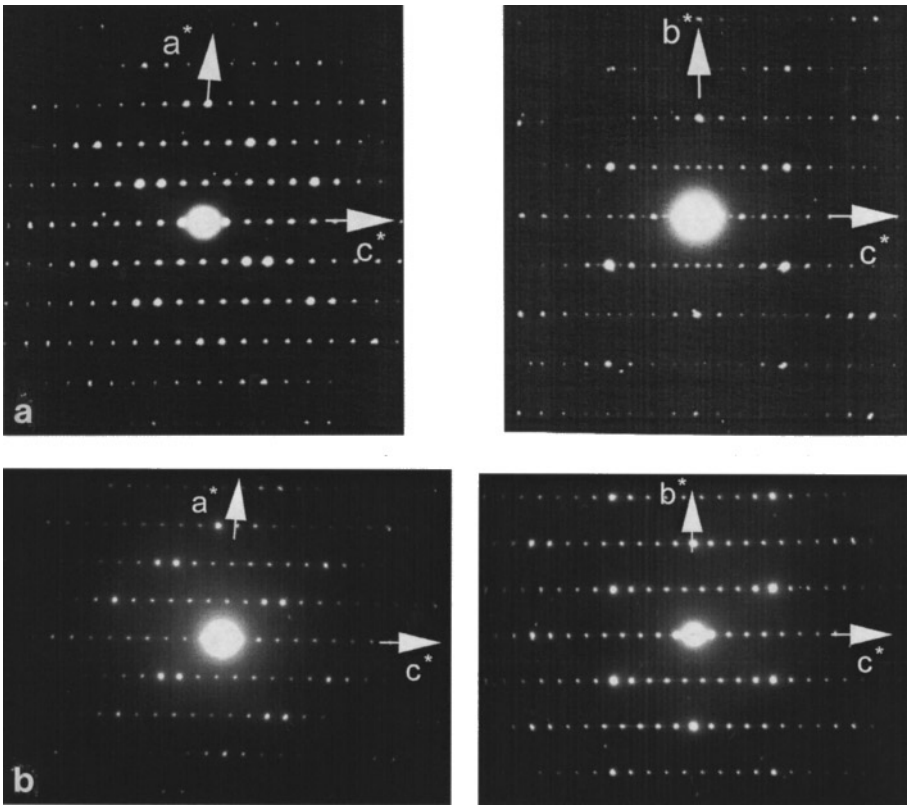

FIG. 1. (a) [010] and [100] electron diffraction patterns for $Pb_xP_4W_{12}O_{44}$ showing the reflection conditions $h0l$ $l = 2n$, $0kl$ none, compatible with $P2_1/c$ space group. $0k0$ dots with odd-k values are due to multiple reflection phenomena. (b) [010] and [100] electron diffraction patterns for $Pb_xP_4W_{14}O_{50}$ showing the reflection conditions $h0l$ $l = 2n$, $0kl$ $k + l = 2n$, compatible with $A2/m$ space group.

into account the HREM image (Fig. 4a), which indeed shows a twinned crystal with an almost planar boundary that can be rather easily modeled (Fig. 4b).

Electrical Resistivity and Magnetic Susceptibility

Single crystals large enough to be used for electrical measurements have been obtained for $m = 7$. The thermal dependence of the normalized resistivity measured in the (**a**, **b**) plane is shown in Fig. 5. The materials are metallic for the entire temperature range explored without visible anomaly as reported for $K_xP_4W_8O_{32}$ (19) (see inset to Fig. 5).

Room temperature resistivity measured in the plane of the platelet is of 8.7 $\mu\Omega \cdot$cm, closed to that observed for $Na_xP_4W_8O_{32}$ and $K_xP_4W_8O_{32}$ single crystals (18, 19).

The magnetic susceptibility measured either for polycrystalline powder samples or for a batch of oriented single crystals exhibits the same behavior down to low temperature (Fig. 6). It tends at high temperature to a small but not zero value ($\approx 10^{-7}$ emu/g), which is typical of Pauli paramagnetism behavior. At low temperatures the susceptibility increases steeply which is likely due to the presence of extrinsic paramagnetic centers or impurities.

TABLE 1
Unit Cell Parameters Refined for $Pb_xP_4W_{2m}O_{8+6m}$ Powder Samples Assuming a Monoclinic Symmetry

m	a(Å)	b(Å)	c(Å)	β(°)
6	6.609(1)	5.297(1)	23.813(5)	93.01(1)
7[a]	6.607(4)	5.317(3)	27.01(2)	96.86(4)
8	6.593(7)	5.343(3)	30.79(3)	101.6(1)
9	6.553(7)	5.302(4)	34.44(3)	97.88(8)
10	6.600(3)	5.309(3)	36.14(2)	95.58(3)

[a] For $m = 7$ the single-crystal X-ray investigation indicates a triclinic symmetry (see Table 2).

Structure Determination

Several crystals corresponding to the members $m = 6$ and $m = 7$ of the series have been obtained in the form of dark blue platelet-like crystals and tested with a Weissenberg camera. For $m = 6$, it was found that most of the crystals were of poor quality, showing either elongated spots and doublets or twins. On the other hand, for $m = 7$ a crystal of

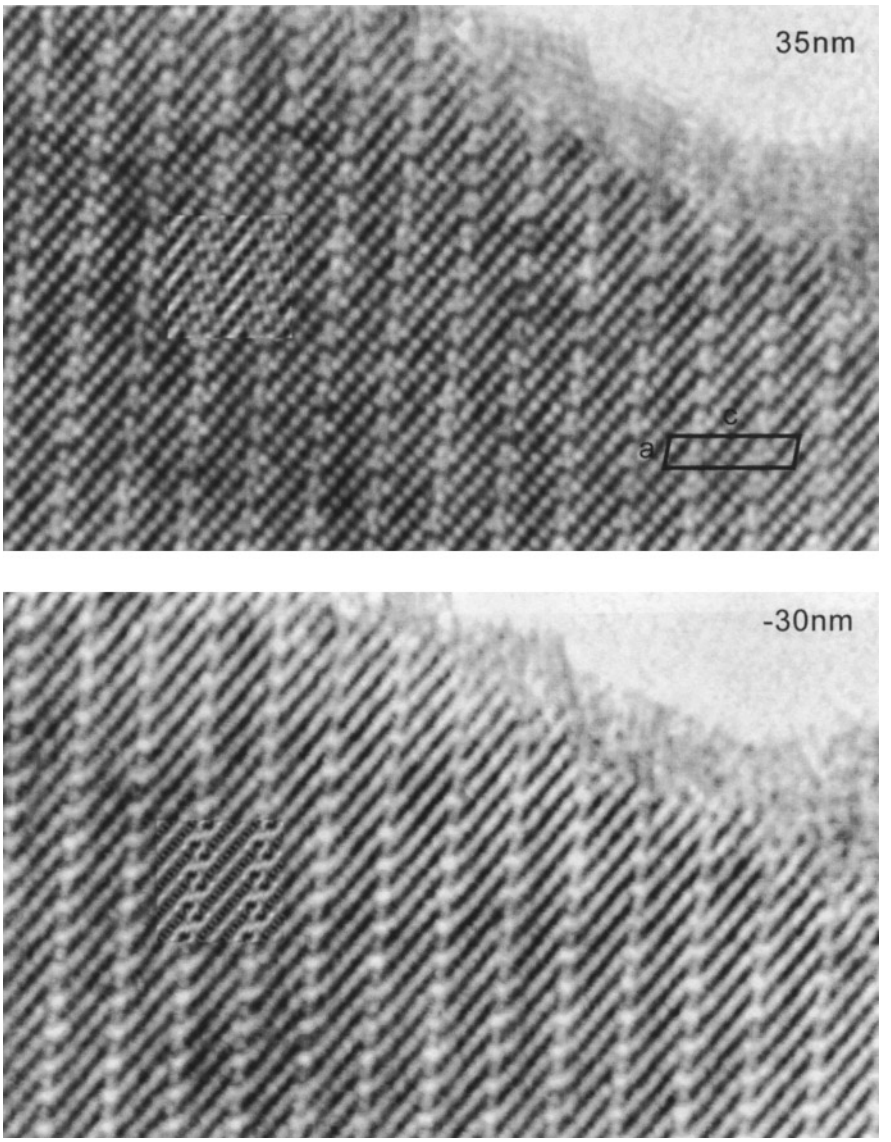

FIG. 2. Two typical focus value [010] HREM images of $Pb_xP_4W_{14}O_{50}$ microcrystal. Calculated images (crystal thickness, 3.9 nm) are inset.

very good quality with sharp spots even for high k values of the Weissenberg levels ($k = 0, 1, 2, 3$) could be selected and used for a precise single-crystal X-ray investigation.

In agreement with ED patterns, Weissenberg photographs indicated a monoclinic symmetry with preliminary unit cell parameters $a \approx 6.6$ Å, $b \approx 5.3$ Å, $c \approx 27.1$ Å, and $\beta \approx 96.2^\circ$. This orientation was chosen for the data collection to allow easier comparison with other members of the $MPTB_h$ family. Systematic absences (hkl: $k + l = 2n + 1$) were consistent with an $A2/m$ point group.

Single-crystal data were then collected under the conditions given in Table 2. The comparison of the collected intensities revealed, however, a triclinic rather than a monoclinic symmetry for which the R_{int} calculated for the equivalent reflections is higher than 0.10. A least-squares refinement of the unit cell parameters based on the more intense 25 reflections and for the angular range $36^\circ < 2\theta < 50^\circ$ leads indeed to the values $a = 6.6015(3)$ Å, $b = 5.3156(4)$ Å, $c = 27.039(2)$ Å, $\alpha = 90.208(6)^\circ$, $\beta = 96.757(5)^\circ$, $\gamma = 89.867(5)^\circ$. The triclinic distortion is thus very weak, explaining why it cannot be detectable on ED patterns (Fig. 1b).

Such a result appeared in agreement with that observed for the Na-based analogue $Na_{1.7}P_4W_{14}O_{50}$ (21). Accordingly the structure refinement was achieved in the nonconventional space group $A\bar{1}$ with atomic positions close to those previously obtained for $Na_{1.7}P_4W_{14}O_{50}$. The refinement rapidly converged to weak values of the reliability factors $R = 2.16\%$ and $R_w = 2.41\%$, with an occupancy

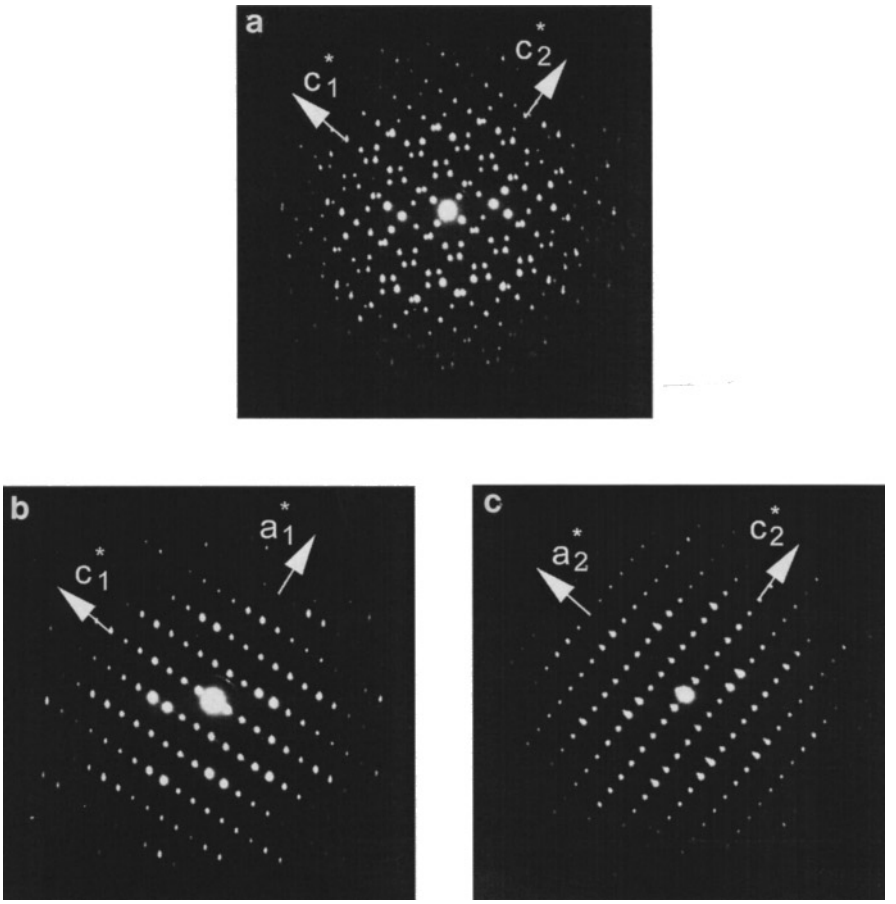

FIG. 3. Electron diffraction patterns of a $Pb_xP_4W_{12}O_{44}$ microcrystal showing two oriented domains: SAED patterns of (a) both domains, (b) domain 1, and (c) domain 2.

rate of $16.55 \pm 0.08\%$ for the Pb^{2+} site, leading to the chemical formula $Pb_{0.66}P_4W_{14}O_{50}$. Final atomic coordinates and equivalent displacement parameters are listed in Table 3. Selected interatomic bond distances are given in Table 4.

DESCRIPTION AND DISCUSSION

Like that of the other members of the $MPTB_h$ series, the crystal structure of $Pb_{0.66}P_4W_{14}O_{50}$ can be described as a stacking of WO_3-type slabs linked by PO_4 tetrahedra arranged in slices parallel to the slabs (Fig. 7). Each WO_3-type slab is built up from parallel strings of three or four WO_6 octahedra sharing corners. All the slabs have exactly the same thickness and the peculiarity of all the compounds belonging to the $MPTB_h$ family lies in the fact that all the strings of octahedra have exactly the same orientation, contrary to the members of $MPTB_p$ family (6–9), where two successive slabs appear as a structural chevron arrangement. The result is the existence of pseudo-hexagonal tunnels where the (*A*) inserted cations (Na^+, K^+, Pb^{2+}) are located.

In fact, the hexagonal shape is only an appearance. The (*A*) cations are actually located inside cages bounded by 18 oxygen atoms which communicate with each other by means of two hexagonal windows and six diamond-shaped windows. These O_{18} cages are made of 8 WO_6 octahedra and 4 PO_4 tetrahedra, all corner sharing (Fig. 8). The length of this cage corresponds approximately to the sum of one height of a WO_6 octahedron and an edge of a PO_4 tetrahedron, therefore about 6.4 Å, and the cross directions to values greater than 3.8 Å. Because of the large size of the cage the inserted (*A*) cations are widely displaced from the center of gravity of the cage: the displacement is thus 1.19 Å for Pb^{2+}, 1.22 Å for Na^+, and 0.95 Å for K^+. As a consequence the oxygen neighborhood is rather anisotropic, involving a (3 + 5) coordination state for Pb^{2+} (Fig. 9a) and (4 + 4) and (6 + 2) coordination states are observed for Na^+ and K^+, respectively (Figs. 9b and 9c).

In fact, all the cations have a tendency to be located on one part of the cage which favors the proximity of PO_4 groups. This can be explained by assuming that formation of the σ(A–O) bond competes with that of (W–O) bonds of

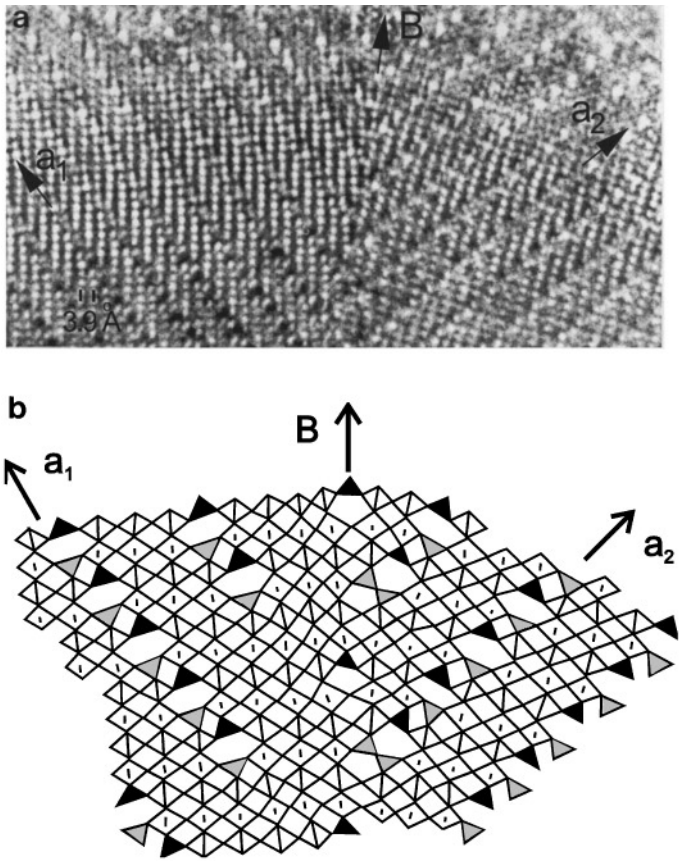

FIG. 4. (a) HREM corresponding image showing that the domain boundary is almost planar. (b) Idealized proposed model involving WO_6 octahedra, PO_4 tetrahedra, P_2O_7 units, and five-sided tunnels at the boundary.

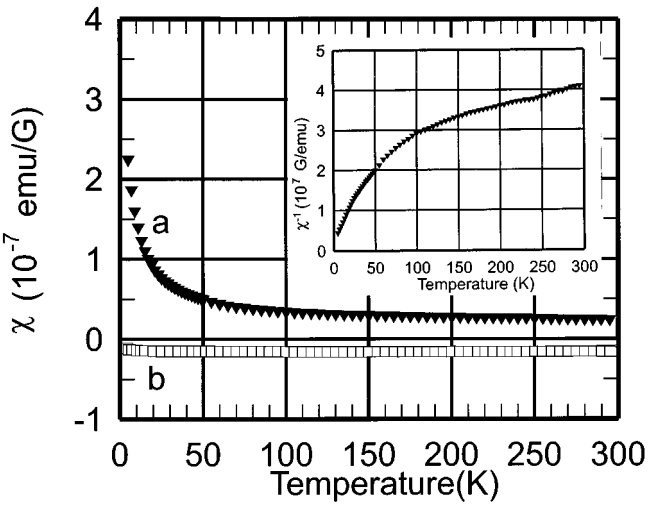

FIG. 6. Thermal dependence of the magnetic susceptibility (a) and of reciprocal magnetic susceptibility (inset) of a powder sample of $Pb_xP_4W_{14}O_{50}$ (applied magnetic field, 0.5 T). The susceptibility curve (b) of the sample holder has been drawn for comparison.

WO_6 octahedra made up of t_{2g} orbitals of W atoms and $2p\pi$ orbitals of oxygen atoms, which is not the case for P–O bonds of PO_4 tetrahedra.

Pb^{2+} cations are thus located in a position closed to that of Na^+ cations, three of the shortest Na–O distances being substituted by Pb–O distances only 0.05 Å longer (2.50, 2.64, and 2.69 Å for Pb^{2+} compared with 2.44, 2.59, and 2.64 Å for Na^+). In the opposite the fourth short 2.51-Å

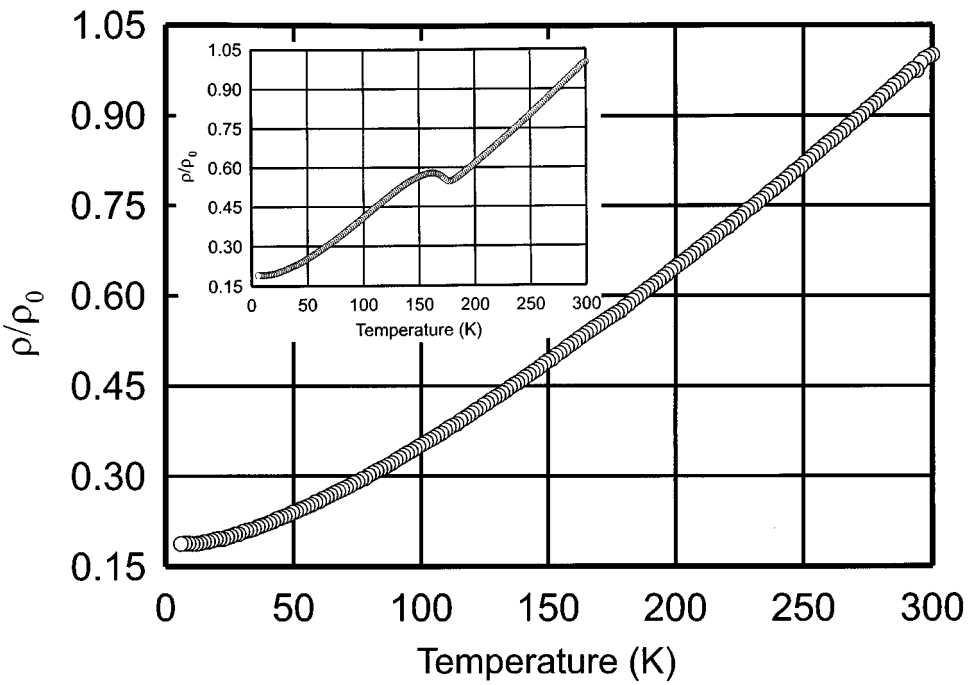

FIG. 5. Thermal dependence of the normalized resistivity for a single crystal of $Pb_xP_4W_{14}O_{50}$. For comparison the electrical behavior of a crystal of $K_xP_4W_8O_{32}$ showing a CDW transition has been reported in the inset [see Ref. (19)].

TABLE 2
Crystal Data, Intensity Measurements and Structure Refinement Parameters for $Pb_{0.66}P_4W_{14}O_{50}$ at 293 K[a]

1. Crystal data	
Crystal symmetry	Triclinic
Space group	$A\bar{1}$
Cell dimensions	$a = 6.6015(3)$ Å, $\alpha = 90.208(6)^\circ$
	$b = 5.3156(4)$ Å, $\beta = 96.757(5)^\circ$
	$c = 27.039(2)$ Å, $\gamma = 89.867(5)^\circ$
Volume ($Z = 1$)	944.2(1) Å^3
Formula weight	3497.6 g mol^{-1}
Crystal form	Platelet delimited by (110), ($\bar{1}$10), ($\bar{1}$00), (1$\bar{1}$0), (00$\bar{1}$), and (001)
Crystal size	$127 \times 102 \times 15$ μm^3
Crystal color	Dark blue
$F(000)$	1550
2. Intensity measurements	
Diffractometer	Enraf-Nonius CAD 4
Radiation	Mo$K\alpha$ ($\lambda = 0.71073$ Å)
Monochromator	Oriented graphite (002)
Scan mode	$\omega - 4\theta/3$
Scan	$1 + 0.35 \tan\theta$ (°)
Recording range θ	$2 \le \theta \le 45$ (°)
Range of h, k, l	$-13 \le h \le 13, -10 \le k \le 10, 0 \le l \le 53$
Standard reflections (every h)	(060) (251) (059)
Intensity decay	$\le 4\%$
Reflections for crystal matrix orientation ($18^\circ < \theta < 25^\circ$)	25
Number of recorded reflections	7746
Absorption correction	Gaussian method
Linear absorption coefficient (for $\lambda = 0.71073$ Å)	456.87 cm^{-1}
Minimum transmission factor	0.0621
Maximum transmission factor	0.5059
Number of independent reflections with $I > 3.0\sigma(I)$	4462 (N)
3. Structure solution and refinement	
Weighting scheme	$w = 1/\sigma^2(F_o)$
R	2.16%
R_w	2.41%
S	1.41
Number of refined parameters	98 (M)
$(\Delta/\sigma)_{max}$	0.002
Extinction coefficient	0.298(2)

[a] $R = (\sum||F_o| - |F_c||)/\sum|F_o|$. $R_w = [\sum w(|F_o| - |F_c|)^2/\sum w|F_o|^2]^{1/2}$. $S = [\sum w(|F_o| - |F_c|)^2/(N - M)]^{1/2}$. Isotropic secondary extinction (Type I) Gaussian distribution.

distance found for Na^+ becomes 2.73 Å for Pb^{2+}, involving a weaker tilting of all WO_6 octahedra. This could be ascribed to the steric effect of the $6s^2$ lone pair of Pb^{2+} as shown in Fig. 8. The location of the lone pair (L) has been established using the program PAIR developed by Le Bellac *et al.* (22) assuming for Pb^{2+} a polarizability of 6.8 (23): it corresponds to a position ($x = 0.297$, $y = 0.05$, $z = 0.266$) that involves a Pb–L distance of 0.85 Å and a PbO_3L tetrahedron in good agreement with previous studies (24, 25).

The K^+ cations exhibit a more homogeneous oxygen environment with distances ranging from 2.64 to 3.06 Å (Fig. 9c) and a perfect symmetrical distribution since the O_{18} cage is cut by a mirror plane. The symmetry is strongly related to the fact that for K-based $MPTB_h$ (26) no tilting of the WO_6 octahedra is observed.

It is thus tempting to suppose that both the size and the stereoactivity of the lone pair play a crucial role in the actual shape of the O_{18} cage. Two arguments seem to favor such an assumption: first, when Na^+ is changed for Pb^{2+} and K^+ the tilting of the WO_6 octahedra (Fig. 10) decreases from about 8.5° to 6.5° and 0°, respectively; second, the mean A–O distance calculated for the eightfold coordination state of the cations increases from 2.67 Å for Na^+ to 2.74 Å for Pb^{2+} and 2.83 Å for K^+, clearly showing that the size of the cage tends to increase.

This can be also be related to the general variation of the unit cell parameters with the value of m which measures the

TABLE 3
Fractional Atomic Coordinates and Atomic Displacement Parameters

Atom	x	y	z	B (Å)^2
W1	0.0(0)	0.0(0)	0.0(0)	0.374(3)[a]
W2	0.69977(2)	0.49986(2)	0.054775(5)	0.327(2)[a]
W3	0.40054(2)	1.00559(2)	0.111960(5)	0.311(2)[a]
W4	0.09048(2)	0.50321(2)	0.168115(5)	0.299(2)[a]
Pb	0.3368(1)	− 0.0141(2)	0.23758(3)	0.85(1)[a]
P	0.2016(1)	0.4828(2)	0.29221(3)	0.225(9)
O1	0.1958(4)	0.0002(5)	0.0602(1)	0.65(3)
O2	0.5(0)	0.5(0)	0.0(0)	0.67(5)
O3	0.8624(4)	0.7226(5)	0.0246(1)	0.65(3)
O4	0.8285(4)	0.2208(5)	0.0315(1)	0.63(3)
O5	0.5615(4)	0.7797(5)	0.0846(1)	0.78(3)
O6	0.5294(4)	0.2795(5)	0.0911(1)	0.65(3)
O7	0.9044(4)	0.5066(5)	0.1142(1)	0.76(4)
O8	0.2638(4)	0.7275(5)	0.1461(1)	0.71(3)
O9	0.2307(4)	0.2304(5)	0.1515(1)	0.76(3)
O10	0.5918(4)	− 0.0023(5)	0.1764(1)	0.90(4)
O11	0.2420(4)	0.5047(5)	0.2377(1)	0.60(3)
O12	0.0617(4)	0.7006(5)	0.3043(1)	1.02(4)
O13	0.1042(4)	0.2280(5)	0.2999(1)	0.83(3)

Atom	U_{11}	U_{22}	U_{33}	U_{12}	U_{13}	U_{23}
W1	0.00500(3)	0.00435(5)	0.005099(2)	0.00013(3)	0.001540(6)	0.000161(8)
W2	0.00414(2)	0.00403(3)	0.004343(1)	0.00002(2)	0.000761(4)	0.000091(6)
W3	0.00383(2)	0.00389(3)	0.004214(1)	0.00006(2)	0.001015(4)	0.000081(6)
W4	0.00390(2)	0.00425(3)	0.003276(1)	0.00003(2)	0.000671(4)	0.000259(5)
Pb	0.0135(1)	0.0097(2)	0.009713(8)	−0.0007(1)	0.00382(3)	−0.00021(4)

[a]Isotropic equivalent ADPs defined as $B_{eq} = (8\pi^2/3)\sum_i\sum_j U_{ij} a_i^* a_j^* a_i a_j$.

TABLE 4
Selected Interatomic Distances (Å) for $Pb_{0.66}P_4W_{14}O_{50}$

W1–O1	1.956(3)	W4–O7	1.793(3)
W1–O1	1.956(3)	W4–O8	1.805(3)
W1–O3	1.896(3)	W4–O9	1.802(3)
W1–O3	1.896(3)	W4–O11	2.024(3)
W1–O4	1.897(3)	W4–O12	2.051(3)
W1–O4	1.897(3)	W4–O13	2.046(3)
W2–O2	1.864(1)	P–O10	1.523(3)
W2–O3	1.855(3)	P–O11	1.534(3)
W2–O4	1.852(3)	P–O12	1.537(3)
W2–O5	1.963(3)	P–O13	1.525(3)
W2–O6	1.968(3)		
W2–O7	1.974(3)	Pb–O8	2.817(3)
		Pb–O9	2.688(3)
W3–O1	1.829(3)	Pb–O10	2.496(3)
W3–O5	1.815(3)	Pb–O11	2.635(3)
W3–O6	1.813(3)	Pb–O11	2.826(3)
W3–O8	2.016(3)	Pb–O11	2.782(3)
W3–O9	2.024(3)	Pb–O12	2.913(3)
W3–O10	2.029(3)	Pb–O13	2.727(3)

thickness of the WO_3-type slabs. As can be seen in Fig. 11 the values reported for the K^+-based compounds are systematically higher than those for the Pb^{2+}- and Na^+-based analogues. However it is worth noting that for all the compounds the a and b parameters do not vary significantly with m, remaining close to $a_p\sqrt{3}$ and $a_p\sqrt{2}$, respectively, where a_p is the perovskite unit cell parameter ($a_p \approx 3.80$ Å). On the other hand the c parameter varies linearly with m according to the expected relation $c = (0.816 a_p * m + 4.90)/\sin\beta$, assuming a monoclinic symmetry.

The fact that no sign of resistivity anomaly can be detected for $Pb_{0.66}P_4W_{14}O_{50}$ single crystals while CDW transitions have been predicted for $MPTB_h$ bronzes from band structure calculations (17) is not well understood at present. Indeed, it should be pointed out that the occupancy

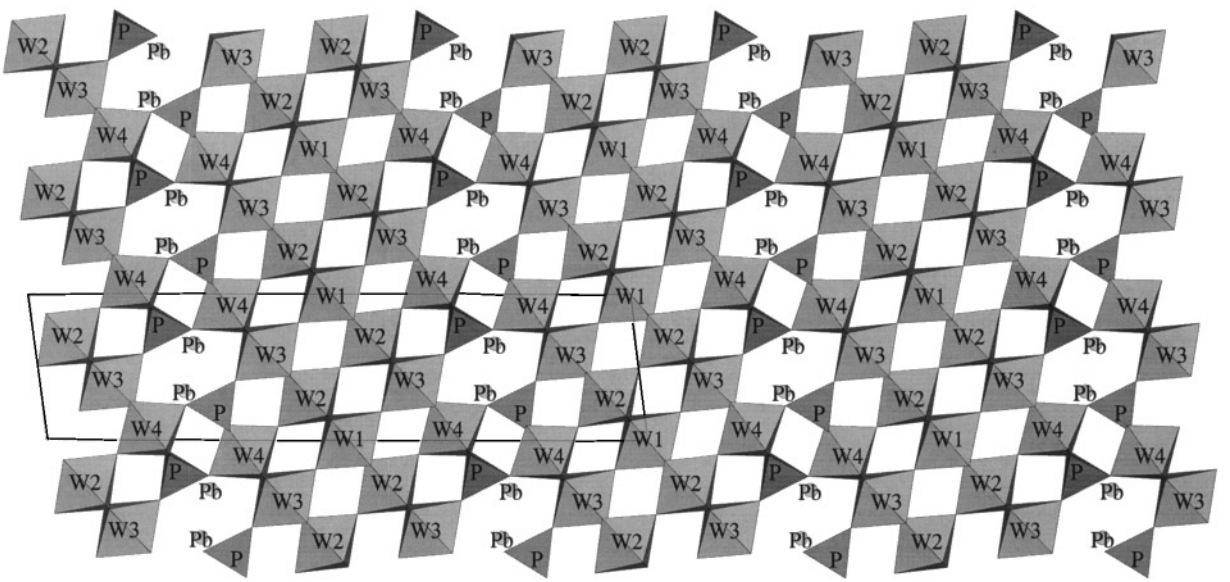

FIG. 7. $Pb_{0.66}P_4W_{14}O_{50}$: projection of the structure along the b axis.

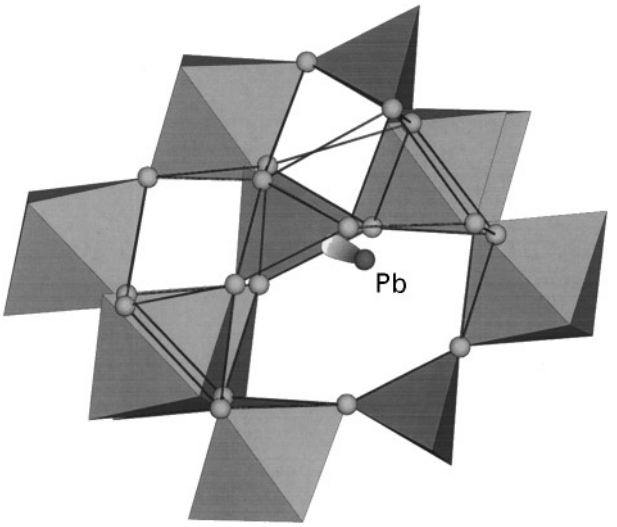

FIG. 8. O_{18} cage drawn from a projection along [010]. The orientation of the $6s^2$ lone pair of Pb^{2+} is indicated.

rate found for Pb^{2+} in the O_{18} cages ($16.55 \pm 0.08\%$) is nearly half that found for K^+ ($32 \pm 2\%$) in $K_xP_4W_8O_{32}$ (19), leading to the same electron band filling.

On the basis of previous results reported for the closely related diphosphate tungsten bronze $CsP_8W_8O_{40}$ (27) the difference in the temperature-dependent behavior of the resistivity for the two compounds $Pb_{0.66}P_4W_{14}O_{50}$ and $K_xP_4W_8O_{32}$ might originate from order–disorder phenomena due to a partial ordering of Pb^{2+} inside the O_{18} cages.

Indeed, it has been shown from diffuse X-ray scattering experiments (28) that the unusual quasi-1D electron transport properties of $CsP_8W_8O_{40}$ might be understood on the basis of a partial ordering of Cs^+ in the octagonal tunnels delimited by the structure (29). In the same way, it should be noted that order–disorder phase transitions have been characterized from electron microscopy investigations performed on $Na_xP_4W_8O_{32}$ and $K_xP_4W_{12}O_{44}$, $MPTB_h$ compounds.

First, for some $Na_xP_4W_8O_{32}$ crystals it has been shown that a symmetry change corresponding to the disappearance on [100] ED patterns of superstructure spots could be induced in the microscope by increasing the intensity of the electron beam (30). Then for $K_xP_4W_{12}O_{44}$ specimens, contrast variations on (010) HREM images of the rows of spots associated with hexagonal tunnels of the structure have been demonstrated to depend on the K^+ occupation ratio

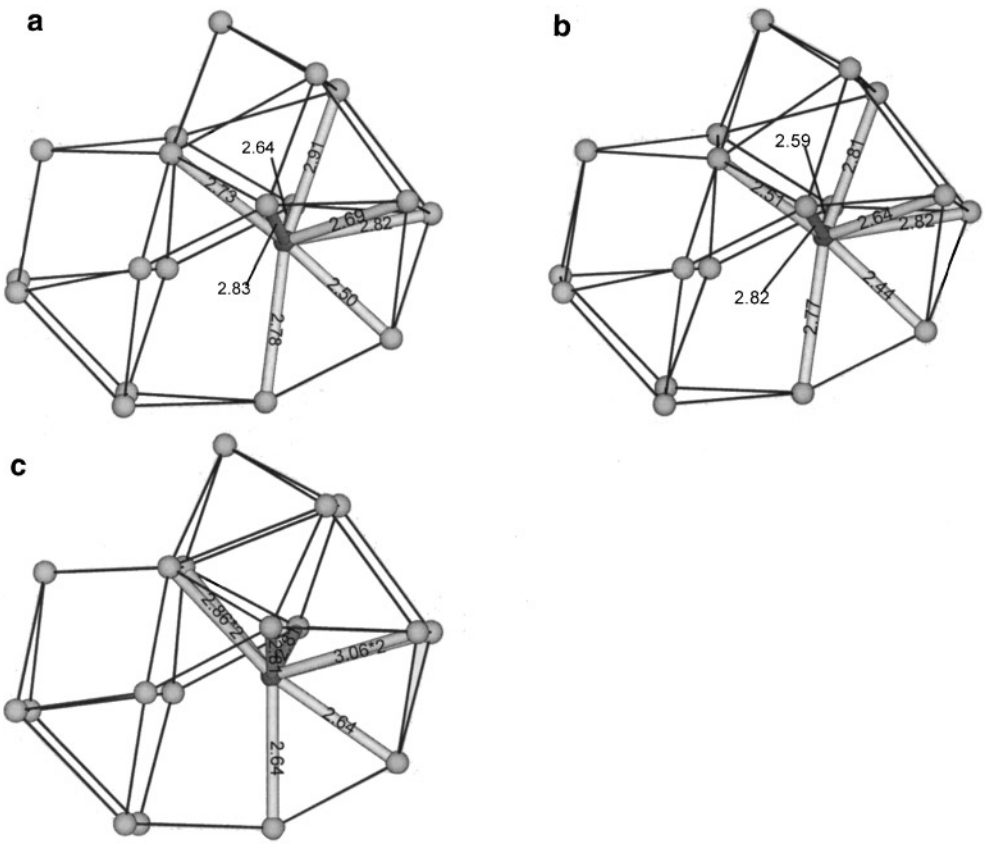

FIG. 9. Eighth nearest oxygen neigbor of Pb^{2+} (a) compared with those of Na^+ (b) and K^+ (c) in MPTBh analogues $A_xP_4W_{14}O_{50}$ (A = Pb, Na, K). Projections along [010].

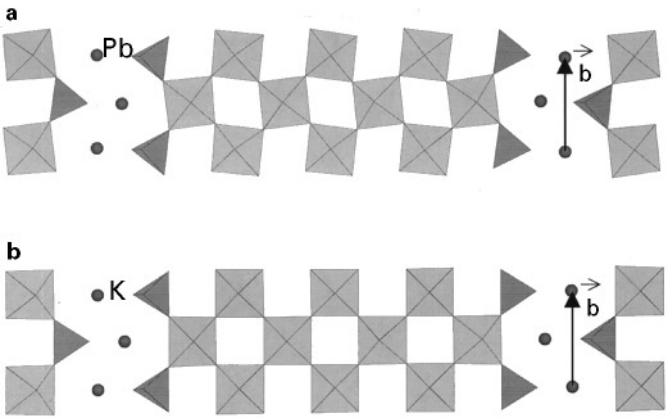

FIG. 10. Projection along [301] of a WO_3-type slab of $Pb_xP_4W_{14}O_{50}$ (a) compared with that of $K_xP_4W_{14}O_{50}$ (b). The WO_6 tilting is about 6.5° with respect to the [010] direction.

x of the O_{18} cages (16). Therefore, it should be assumed that for Pb-MPTB$_h$ similar order–disorder phenomena might exist.

In this assumption the room temperature phase of $Pb_{0.66}P_4W_{14}O_{50}$ should be considered a low-temperature form with a partial ordering of Pb^{2+} cations in the O_{18} cages. From a structural point of view, such behavior would be difficult to prove since the expected transition would transform a pseudo-monoclinic lattice into a real one without a significant change in the diffracted intensities and without modification of the extinction rules. Some CBED observations of (b^*, [$h0h$]*) planes have been made at low temperature (liquid nitrogen), and in agreement with CBED simulations based on the true triclinic structure and modeled monoclinic structure, it appeared that such a tiny structural modification (involving pseudo-symmetries) could not be induced through this method.

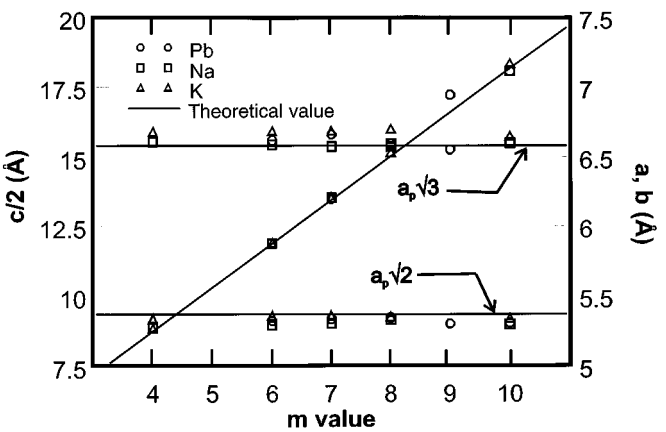

FIG. 11. Unit cell parameters for the MPTB$_h$ series $A_x(PO_2)_4(WO_3)_{2m}$ (A = Pb, Na, K) as a function of the thickness m of the WO_3-type slabs. The continuous line drawn for $c/2$ corresponds to $c/2 = 1.57 * m + 2.48$ (Å).

CONCLUDING REMARKS

A new series of monophosphate tungsten bronzes $Pb_x(PO_2)_4(WO_3)_{2m}$ involving Pb^{2+} cations in pseudo-hexagonal tunnels has been synthesized for $6 \leq m \leq 10$. Crystal structure calculations performed for $m = 7$ have shown that the occupancy rate of Pb^{2+} is roughly half those observed for Na^+- and K^+-based analogues leading to similar electron band filling. Resistivity measurements carried out between 300 and 4.2 K show metallic and quasi-2D behavior.

Contrary to $K_xP_4W_8O_{32}$, no CDW formation even so predicted from band structure calculations has been detected for the investigated temperature range 4.2–300 K.

We suggest that for lead-based compounds, possible cation ordering in the hexagonal tunnels could play a role in the temperature onset of electronic instabilities. Further work is necessary, however, to increase our understanding of resistivity anomalies in this new MPTB$_h$ class of low-dimensional conductors.

REFERENCES

1. A. Rötger, C. Schlenker, J. Dumas, E. Wang, Z. S. Teweldemedhin, and M. Greenblatt, *Synth. Met.* **55–57,** 2670 (1993).
2. A. Rötger, J. Lehmann, C. Schlenker, J. Dumas, J. Marcus, Z. S. Teweldemedhin, and M. Greenblatt, *Europhys. Lett.* **25** (1), 23 (1994).
3. C. Le Touze, G. Bonfait, C. Schlenker, J. Dumas, M. Almeida, M. Greenblatt, and Z. S. Teweldemedhin, *J. Phys. I Fr.* **5,** 437 (1995).
4. A. Ottolenghi, P. Foury, J. P. Pouget, Z. S. Teweldemedhin, M. Greenblatt, D. Groult, J. Marcus, and C. Schlenker, *Synth. Met.* **70,** 1301 (1995).
5. C. Hess, C. Schlenker, J. Dumas, M. Greenblatt, and Z. S. Teweldemedhin, *Phys. Rev. B* **54,** 4581 (1996).
6. J. P. Giroult, M. Goreaud, Ph. Labbé, and B. Raveau, *Acta Crystallogr. Sect. B* **37,** 2139 (1981).
7. A. Benmoussa, Ph. Labbé, D. Groult, and B. Raveau, *J. Solid State Chem.* **44,** 318 (1982).
8. B. Domengès, M. Hervieu, B. Raveau, and R. J. D. Tilley, *J. Solid State Chem.* **54,** 10 (1984).
9. Ph. Labbé, M. Goreaud, and B. Raveau, *J. Solid State Chem.* **61,** 324 (1986).
10. A. Ottolenghi and J. P. Pouget, *J. Phys. I Fr.* **6,** 1059 (1996).
11. C. Schlenker, C. Le Touze, C. Hess, A. Rötger, J. Dumas, J. Marcus, M. Greenblatt, Z. S. Teweldemedhin, A. Ottolenghi, P. Foury, and J. P. Pouget, *Synth. Met.* **70,** 1263 (1995).
12. C. Schlenker, C. Hess, C. Le Touze, and J. Dumas, *J. Phys. I Fr.* (Schegolev Memorial Volume) **6,** 2061 (1996).
13. J. Lehmann, C. Schlenker, C. Le Touze, A. Rötger, J. Dumas, J. Marcus, Z. S. Teweldemedhin, and M. Greenblatt, *J. Phy. IV Fr.* **3,** 243 (1993).
14. J. P. Giroult, M. Goreaud, Ph. Labbé, and B. Raveau, *J. Solid State Chem.* **44,** 407 (1982).
15. A. Benmoussa, D. Groult, Ph. Labbé, and B. Raveau, *Acta Crystallogr. Sect. C* **40,** 573 (1984).
16. (a) B. Domengès, M. Hervieu, B. Raveau, and M. O'Keeffe, *J. Solid State Chem.* **72,** 155 (1988). (b) B. Domenges, M. Hervieu, and B. Raveau, *Acta Crystallogr. Sect. B* **46,** 610 (1990).
17. E. Canadell and M. H. Whangbo, *Phys. Rev. B* **43,** 1894 (1991).
18. E. Wang, M. Greenblatt, I. E. Rachidi, E. Canadell, and M. H. Whangbo, *J. Solid State Chem.* **81,** 173 (1989).

19. P. Roussel, D. Groult, C. Hess, Ph. Labbé, and C. Schlenker, *J. Phys. Condensed Matter* **9,** 7081 (1997).
20. V. Petricek and M. Dusek, JANA98, Institute of Physics, Prague, 1997.
21. M. Lamire, Ph. Labbé, M. Goreaud, and B. Raveau, *J. Solid State Chem.* **66,** 64 (1987).
22. D. Le Bellac, J. M. Kiat, and P. Garnier, *J. Solid State Chem.* **114,** 459 (1995).
23. D. R. Lide (Ed.) "Handbook of Chemistry and Physics," 72nd ed. CRC Press, Boca Raton, FL, 1991.
24. J. Galy and R. Enjalbert, *J. Solid State Chem.* **44,** 1 (1982).
25. O. Mentre and F. Abraham, *J. Solid State Chem.* **125,** 91 (1996).
26. B. Domengès, M. Goreaud, Ph. Labbé, and B. Raveau, *J. Solid State Chem.* **50,** 173 (1983).
27. E. Wang and M. Greenblatt, *J. Solid State Chem.* **76,** 340 (1988).
28. P. Foury, J. P. Pouget, E. Wang, and M. Greenblatt, *Synth. Met.* **41–43,** 3973 (1991).
29. M. Goreaud, Ph. Labbé, and B. Raveau, *J. Solid State Chem.* **56,** 41 (1985).
30. A. Benmoussa, D. Groult, and B. Raveau, *Rev. Chim. Min.* **21,** 710 (1984).